ACS OMEGA

http://pubs.acs.org/journal/acsodf

Article

Structural Characterization of the Human Cytosolic Malate Dehydrogenase I

William M. McCue and Barry C. Finzel*

Cite This: *ACS Omega* 2022, 7, 207−214

Read Online

ACCESS | Metrics & More | Article Recommendations | Supporting Information

ABSTRACT: The first crystal structure of the human cytosolic malate dehydrogenase I (MDH1) is described. Structure determination at a high resolution (1.65 Å) followed production, isolation, and purification of human MDH1 using a bacterial expression system. The structure is a binary complex of MDH1 with only a bound malonate molecule in the substrate binding site. Comparisons of this structure with malate dehydrogenase enzymes from other species confirm that the human enzyme adopts similar secondary, tertiary, and quaternary structures and that the enzyme retains a similar conformation even when nicotinamide adenine dinucleotide (NAD^+) is not bound. A comparison to the highly homologous porcine (*sus scrofa*) MDH1 ternary structures leads to the conclusion that only small conformational differences are needed to accommodate binding by NAD^+ or other NAD^+ mimetics. Conformational differences observed in the second subunit show that the NAD^+ binding elements are nevertheless quite flexible. Comparison of *h*MDH1 to the human mitochondrial malate dehydrogenase (*h*MDH2) reveals some key differences in the $\alpha7-\alpha8$ loop, which lies directly beneath the substrate binding pocket. These differences might be exploited in the structure-assisted design of selective small molecule inhibitors of *h*MDH1, an emerging target for the development of anticancer therapeutics.

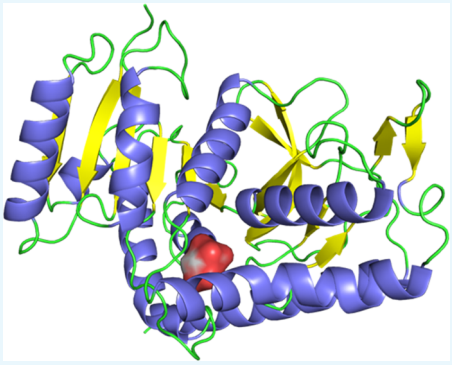

1. INTRODUCTION

Malate dehydrogenases (MDH) belong to the family of nucleotide-binding proteins referred to as nicotinamide adenine dinucleotide (NAD)-dependent dehydrogenases or oxidoreductases.[1] This enzyme family includes the lactate dehydrogenases (LDHs), the liver alcohol dehydrogenases (LADHs), and the glyceraldehyde-3-phosphate dehydrogenases (GADPHs), among others.[1] Malate dehydrogenase reversibly converts malate to oxaloacetate with the use of NAD^+/NADH as a cofactor in the tricarboxylic acid cycle.[2] Most cells contain two main isoforms, which differ in their cellular compartmentalization and role in cellular processes: in eukaryotes, malate dehydrogenase II (MDH2) is found in the mitochondrial matrix where it is involved in the citric acid cycle, while malate dehydrogenase I (MDH1) is localized in the cytosol where it is important to the malate/aspartate shuttle of the urea cycle.[2]

Malate dehydrogenase I is overexpressed in a variety of cancers, and MDH1 amplification in human tumors is a common aberration that correlates with poor prognosis.[3] A hallmark of cancer cells is the increased glucose consumption required for the production of macromolecules necessary for growth and division.[4] Cytosolic NAD levels are independent of mitochondrial NAD levels involved in the electron transport chain.[5] Increased cytosolic concentrations of NAD are necessary to maintain the enhanced glycolysis of proliferating cancer cells, which has largely been attributed to the production of lactate through LDH activity.[4,5] Recently, it has been shown through the use of glucose isotopomer tracing in N5 cells that MDH1 supports LDH in the replenishing of cytosolic NAD.[6] The same study also showed that Jurkat cells with MDH1 knocked out (MDH1 KO.1 and MDH1 KO.2) show slower proliferation and glucose consumption than cells with functional MDH1.[6] This observation leads to the possibility that an MDH1-selective inhibitor, used either alone or in combination with LDH inhibitors, might slow tumor growth and cancer progression in patients.

Structural studies employing crystallography have been used to study malate dehydrogenase enzymes. Structures are known for MDH2 enzymes from *Escherichia coli*,[7−9] plants,[10] and mammals.[11] These MDH2 enzymes all share high sequence homology to human MDH2 (55−95%) but are distinct from MDH1 enzymes that share lower homology (25−30%). Human MDH1 and MDH2 share only 26% sequence identity. Cytosolic MDH1 enzyme structures have been investigated from several species including bacteria[12,13] and plants.[14] These enzymes share good sequence homology with the human MDH1 (50−62% identity). Collectively, this work has

Received: August 13, 2021
Accepted: December 9, 2021
Published: December 28, 2021

https://doi.org/10.1021/acsomega.1c04385
ACS Omega 2022, 7, 207−214

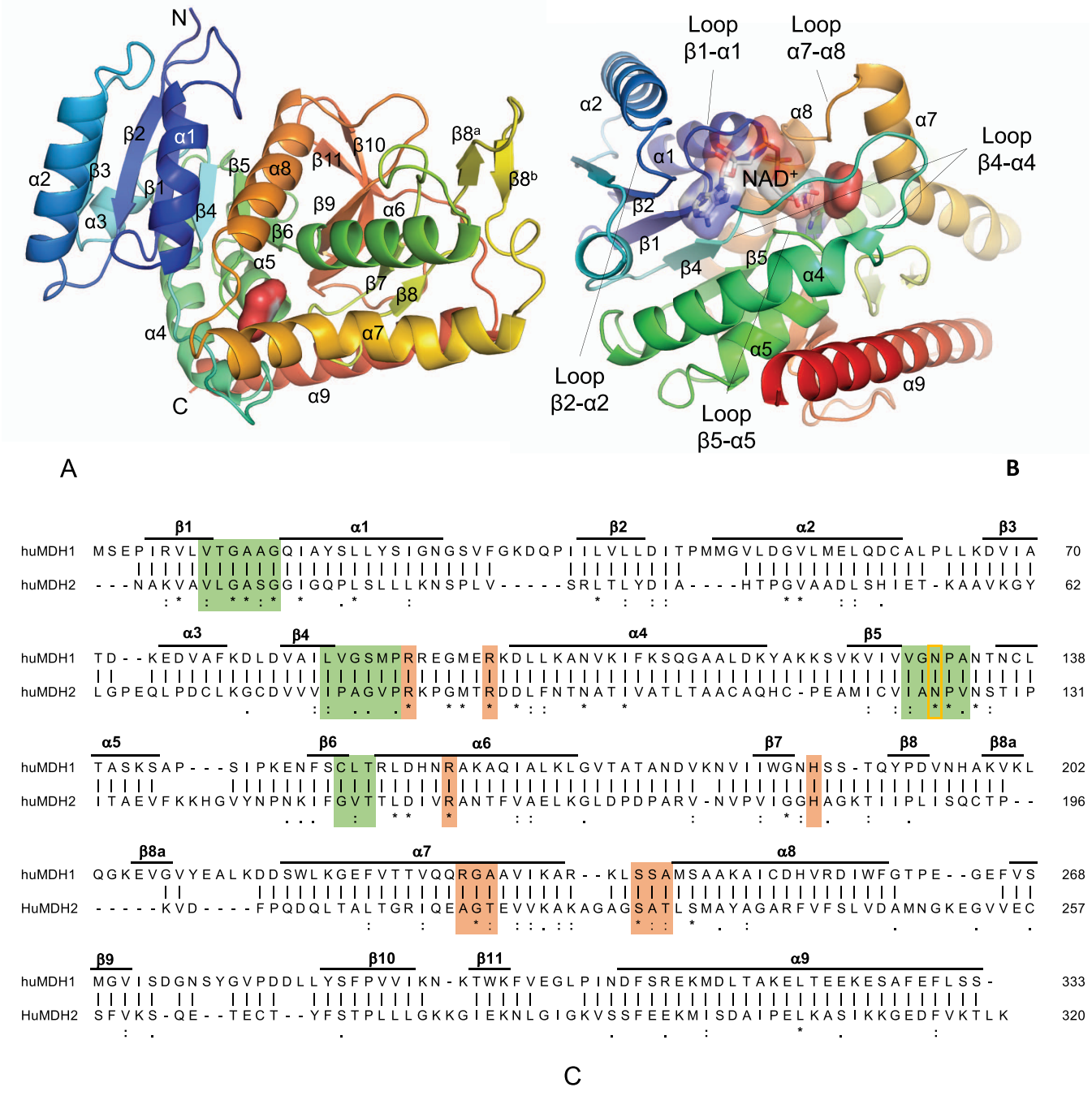

Figure 1. *h*MDH1 monomer fold and secondary structure. (A) The monomer structure illustrated with gradient coloring to show the progression of the chain from N (blue) to C (red) terminus. Consensus secondary structure elements are identified. The bound malonate is within the CPK-colored surface. (B) An alternate view that focuses on elements of structure surrounding the predicted NAD^+ binding site (shown with the transparent surface for positional reference only). Loops prominently referred to in the Results and Discussion section are identified. (C) A structure-based alignment of human MDH1 and MDH2. Secondary structure assignments in *h*MDH1 are identified across the top. Vertical lines joining amino acids in the two sequences denote a 1:1 correspondence in the position of residues in the structures of the two enzymes. Boxes identify cofactor (green) and ligand (orange) binding motifs. Sequence conservation marks displayed (*,:,.) are from a Clustal-Omega multiple sequence alignment of MDHs with known structures in the PDB.

confirmed that the structures are quite homologous across all species. All MDH enzymes share a common Rossmann fold motif characteristic of other NAD(P) binding dehydrogenases,[15] a common dimeric quaternary structure, and highly similar NAD^+/NADH binding sites and mechanisms of catalysis.

Banaszak's group at the University of Minnesota completed some of the first high-resolution crystallographic studies with porcine (*sus scrofa*) MDH1 over 25 years ago.[16,17] That enzyme shares a very high (95%) sequence identity with the human enzyme, but to date, no human MDH1 structure has been reported. Given the renewed interest in *h*MDH1 as a possible therapeutic target, we have sought to obtain a crystal structure of the human enzyme to enable the direct structure-aided design of an *h*MDH1 inhibitor. Here, we report the first structure of the cytosolic human malate dehydrogenase I and

https://doi.org/10.1021/acsomega.1c04385
ACS Omega 2022, 7, 207−214

compare it to previously determined structures of other homologous cytosolic MDHs and also to the structure of the human mitochondrial MDH (*h*MDH2). The monoclinic crystal form with malonate but no NAD^+/NADH bound provides a unique view of this emerging target for pharmaceutical development.

2. RESULTS AND DISCUSSION

2.1. Expression, Purification, Activity, and Crystallization of *h*MDH1. A modified pGS-21a plasmid was engineered with a tobacco etch virus (TEV) cleavage site, and the human gene *mdhI* was codon-optimized *mdh*1 for bacterial expression and cloned into the modified plasmid. The rationale behind the engineered plasmid was to use codon optimization and a solubility tag glutathione S-transferase (GST) to increase the likelihood of soluble protein after lysis. A TEV cleavage site was included for easy cleavage of the solubility tag from the isolated protein. The combination of the solubility tag and codon optimization yielded soluble protein after cell lysis that was found to bind to the nickel column. TEV protease was able to cleave the GST-tag from *h*MDH1, which could then be further purified through a second nickel column. (GST and His-tagged TEV protease adhered to the column, while cleaved *h*MDH1 did not.) Finally, size exclusion chromatography was employed to ensure the highest possible protein purity for crystallographic and enzymatic studies.

Following isolation of the purified MDH1, the protein was tested in a spectrometric activity assay quantifying the conversion of NADH to NAD^+. By varying enzyme concentration and using oxaloacetate as a substrate, the V_{max} observed is 0.0012 mM/sec, and the K_m observed is 0.00041 mM (Supporting Figure S2). Controls affirm that the oxidation of NADH to NAD^+ was a direct result of *h*MDH1 activity. The oxidation of NADH in the absence of protein was not observed, showing that the conversion of NADH to NAD^+ was a direct result of *h*MDH1. The enzyme is considerably more active than previously reported for *sus scrofa* MDH1 (K_m = 0.036 mM).[29]

Following the confirmation of enzymatic activity, MDH1 crystallography was attempted using previously established conditions for *ss*MDH1 due to the high sequence similarity. Microcrystalline material grew after several days, but to generate more robust and larger crystals, alternate buffer conditions were explored. Previous researchers identified malonate (pH range 4−8) as a good buffer for the crystallization of LDHA, another member of the oxidoreductase family, so malonate was substituted for *N*-(2-hydroxyethyl)piperazine-*N*′-ethanesulfonic acid (HEPES) in crystal optimization.[19,20] Following several rounds of seeding, diffraction quality crystals were successfully generated.

2.2. Secondary, Tertiary, and Quaternary Structures of *h*MDH1. The *h*MDH1 crystal was found to have $P2_1$ symmetry with two protein molecules (the functional biological unit) in the asymmetric unit, and the structure has been solved and refined to a 1.65 Å resolution (Supporting Table S1). Each monomer adopts the Rossmann fold characteristic of other NAD(P) binding dehydrogenases,[15] composed of 9 α-helices and 11 β-strands conserved in all MDH structures (Figure 1A). A lengthy sequence insertion between β8 and α7 of MDH1 enzymes gives rise to an additional β pair ($\beta 8^a$−$\beta 8^b$) curled into the β8−α7 loop not present in MDH2 enzymes. This insertion is revealed in the comparison of *h*MDH1 and *h*MDH2 sequences in Figure 1.

The site of NAD^+/NADH binding in this family of structures lies at the meeting of loops at the edge of the large parallel β sheet within this fold. Loops β1−α1 and β2−α2 support the adenosine diphosphate, β5−α5 cradles the nicotinamide nucleoside, and β4−α4 provides a sort of cap that lays over the cofactor. Substrates (malate or oxaloacetate) bind just to the side of the nicotinamide base, pinched between α helices α7 and α8, held in precise position by H-bonds to universally conserved residues (Arg92, Arg98, Asn131, and His187).

Monomers assemble into biologically relevant homodimers, forming a helical bundle with α1 and α8 replicated across a noncrystallographic twofold axis and winged with extensive contacts between α2 and α7 of opposite monomers (Supporting Figure S3A). The details of this monomer−monomer interface have been exhaustively described previously for the porcine MDH1 structure.[16] There is no direct contact between active sites in the two monomers, but previous work has shown that MDH1 functions as a dimer in solution and disruption of this interaction along the dimer interface could potentially perturb the enzymatic function.[2] While the two monomers are in distinctly different crystallographic environments in our structure, they are quite similar overall (rmsd 0.192 Å). Crystal packing does influence conformational flexibility in this crystal form. The crystallographic B-factors of α-carbons throughout the structure are illustrated in Supporting Figure S3B. Large B-factors are observed for residues 203−205 in subunit A. Amino acids in this region are modeled with lower occupancy (0.5) as positive difference peaks were observed in the $2F_o-F_c$ map but little electron density was observed in the F_o-F_c map. The majority of the important β4−α4 loop (residues 92−99) is disordered in subunit B and cannot be modeled; there is no interpretable electron density for this loop. The rest of the structure is well ordered, with 98% of the amino acids showing favorable torsional angles according to Ramachandran analysis with no outliers.

2.3. NAD^+/NADH Binding Site. The structure reported here has neither NAD^+/NADH nor a substrate bound. We have tried to form binary complexes with NADH and ternary complexes with NADH and oxaloacetate by either soaking or cocrystallization under similar conditions, but these efforts have not yet been successful. The ternary complex of *Sus scrofa* (porcine) MDH1 provides a good basis for predicting where cofactor and substrate might be when bound together in *h*MDH1 and for identifying conformational differences in the *h*MDH1 crystal form that might prevent cofactor binding. To create a predictive model for NAD^+ binding, the highly conserved structural motifs in *h*MDH1 associated with NAD^+ binding in all other MDHs (those amino acids identified within green and orange boxes in the sequence alignment of Figure 1C) were superimposed onto the analogous residues of the *ss*MDH1 ternary complex structure (PDBid: 5MDH), resulting in an rms difference in backbone atoms of only 0.24 Å. The tNAD and a substrate mimetic (α-ketomalonate) positions were then adopted for inclusion in a *h*MDH1 ternary complex (Figure 2).

In the *ss*MDH1 complex (Figure 2A), hydrogen bonds from the backbone of the β1−α1 loop including Gly13 and Gly14 anchor the adenosine ribonucleotide, side chains of Ser89 and Asn131 engage the nicotinamide ribose, and His181 is H-bonded to the nicotinamide amide. The β2−α2 loop closes the adenosine side of the NAD binding pocket, with H-bonds from

https://doi.org/10.1021/acsomega.1c04385
ACS Omega 2022, 7, 207−214

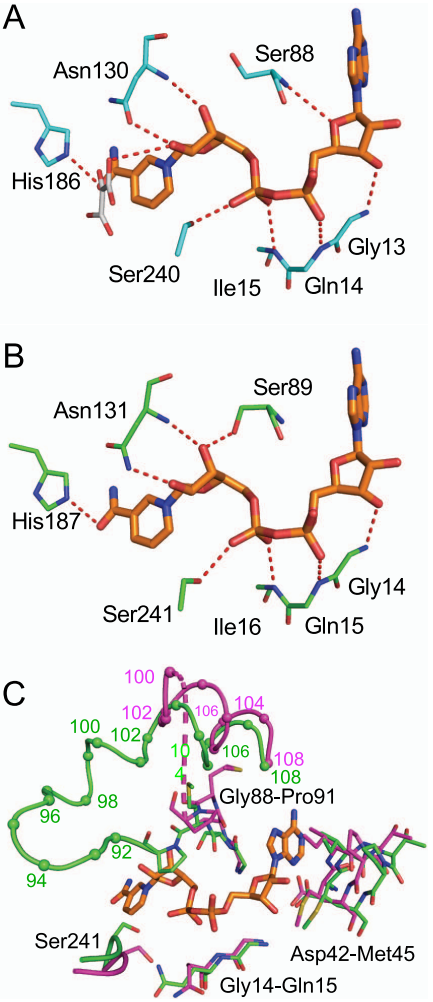

Figure 2. Comparison of NAD^+ binding in the porcine MDH1 complex (PDBId 5MDH) and *h*MDH1 homology model. (A) Prominent H-bonds anchor the tetrahydroNAD (orange) in the *ss*MDH1 structure. Substrate mimetic α-ketomalonate (white) binds beside the nicotinamide in this ternary complex. Interactions between the adenosine ribose and Asp41 are not shown. (B) Predicted NAD^+ binding in *h*MDH1. All of the same H-bonding should be possible in *h*MDH1 subunit A with no conformational change. (C) Comparison of the cofactor binding pocket of *h*MDH1 subunit A (green) and *h*MDH1 subunit B (magenta).

Asp41 to the adenylate ribose (not shown). The *h*MDH1 structure is poised to accept NAD^+/NADH in this same position with minimal conformational adaptation (Figure 2B). All interactions should be preserved except the H-bond to Ser88, which is flipped to a different rotamer orientation in *h*MDH1 when NAD^+ is absent.

The binding elements in subunit B are not well positioned for cofactor binding, however (Figure 2C). As mentioned above, residues 92−98 are completely disordered. While this loop makes little direct contact with NAD^+, it forms the floor of the substrate binding pocket beneath the nicotinamide ring, and substrates typically H-bond to the cofactor. The Gly14−Gln15 amide bond in subunit B is rotated roughly 90 degrees, so that the carbonyl is directed away from the phosphate of NAD^+ to which it should H-bond. Asp42−Met45 and Gly88−Pro91 have all shifted into the NAD^+ binding space, effectively shrinking the binding pocket.

We have examined the crystal packing in the vicinity of NADH binding sites in both subunits, but there is no simple explanation for these conformational differences; no intermolecular interactions exist to prevent subunit B from adopting a conformation similar to that seen in subunit A or *vice versa*. It is interesting that structural flexibility exists, as it affirms the possibility that small molecules might be identified that bind and stabilize conformations of *h*MDH1 that cannot support cofactor binding.

2.4. Malonate Lies in Substrate Binding Pocket. Electron density present in the substrate binding pocket of subunit A can be attributed to malonate (Supporting Figure S2), a component of the buffer for crystallization. No comparable density is found in subunit B, which is less well ordered. Arg92 and Arg98, which figure prominently in positioning substrate molecules, are completely disordered in subunit B as discussed above.

Malonate has been modeled in the *h*MDH1 complex in two different conformations with half occupancy (conformer A and conformer B). The hydrogen bonding stabilizing each conformation is shown in Figure 3A. In both conformations, one carboxylate in this symmetric molecule is positioned opposite the plane of the Arg92 guanidinium to which it is H-bonded. In conformation A, the other carboxylate interacts with Arg162, Arg98, and Ser242. In conformation B, this carboxylate is rotated to hydrogen bond with His187 and the secondary amine in Arg98. These interactions collectively

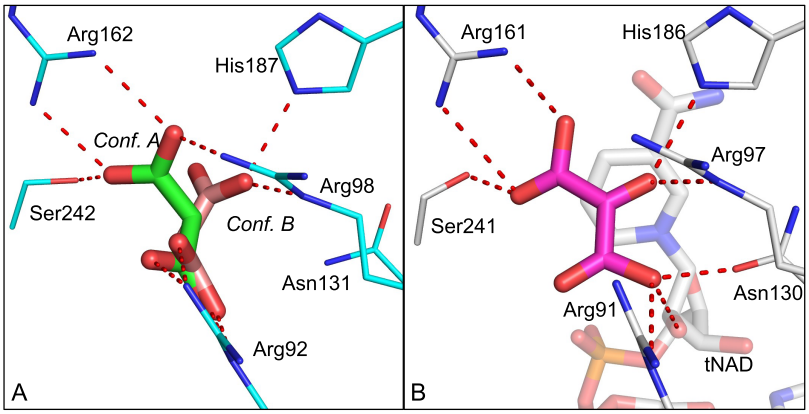

Figure 3. Comparison of ligand binding. (A) Hydrogen bonding to malonate by *h*MDH1. (B) Hydrogen bonding to α-ketomalonate by *ss*MDH1 (PDBId: 5MDH).

https://doi.org/10.1021/acsomega.1c04385
ACS Omega 2022, 7, 207−214

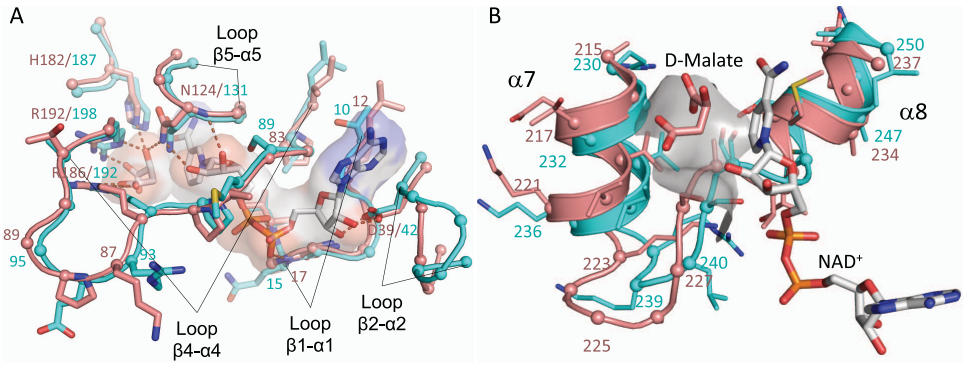

Figure 4. Comparison of *h*MDH1 to *h*MDH2. *h*MDH2, NAD^+, and D-malate are from the ternary *h*MDH2 complex (PDBid: 2dfd). (A) Conservation of structural features needed for cofactor and substrate binding. *h*MDH2 structural features involved in the binding of NAD^+ (white with surface) include H-bonds to Asp39 of loop $\beta2-\alpha2$, Asn124 of loop $\beta5-\alpha5$, and extensive contacts with loop $\beta4-\alpha4$. D-Malate (also white) of the *h*MDH2 complex is held by multiple H-bonds to Asn124, His182, and Arg186 and Arg192 of loop $\beta5-\alpha5$. All of these side chains are conserved and occupy comparable positions in the *h*MDH1 structure, despite the overall low sequence homology and the absence of bound NAD^+. Malonate bound to *h*MDH1 is not shown for clarity. (B) Comparison of the $\alpha7-\alpha8$ loop in *h*MDH1 (cyan) vs *h*MDH2 (salmon). The portion of this loop that should contact the bound malate is illustrated with the fragment of surface (gray).

mimic those observed with more natural substrates and substrate analogues that have additional hydrogen bond acceptors that can make both sets of interactions, such as those observed in the porcine MDH1 complex with α-ketomalonate (PDBid: 5MDH) (Figure 3B). Interestingly, malonate binds in this pocket even in the absence of the NAD^+ cofactor. In the α-ketomalonate complex, one oxygen of the carboxylate is able to hydrogen bond with an exocyclic oxygen of the nicotinamide ribose. We could find no other example of a malate dehydrogenase structure in the PDB that includes a bound substrate analogue in the absence of NAD^+/NADH.

2.5. Differences between Human Cytosolic and Mitochondrial MDH. Any successful targeting *h*MDH1 for therapeutic purposes will require that some degree of selectivity be achieved over the mitochondrial MDH (*h*MDH2). While it has never been described in detail, a high-resolution (1.9 Å) structure of a ternary complex of *h*MDH2 was solved in 2006 by the Structural Biology Consortium and deposited in the PDB with accession code 2DFD. Its existence affords an opportunity for a detailed comparison to the *h*MDH1 enzyme. The structure-based alignment of residues with PDBeFold[18] results in the pairwise alignment of sequences illustrated in Figure 1C and an rmsd of paired backbone atoms of 2.0 Å. However, the superposition of only the NAD^+ binding substructures identified in Figure 1B shows that those substructures are conserved with higher homology (rmsd 0.79Å) (Figure 4). While there are some specific sequence differences including a nonconservative $^{hMDH1}Glu_{94}$ to Pro substitutions in the $\beta4-\alpha4$ loop, and the deletion of several residues from the $\beta2-\alpha2$ loop in *h*MDH1, all of the important hydrogen bond donors and acceptors that anchor NAD^+ in *h*MDH2 are in a position to do so in the same way in *h*MDH1 (Figure 4A). Amino acids Asp41, Asn131, Arg192, and Arg98 and the $\beta1-\alpha1$ loop can all be expected to make comparable H-bonds to secure cofactor binding. Both enzymes also have a histidine (His182/187) positioned to interact with the bound malate.

One feature stands out as potentially relevant to prospects for selective inhibitor design in the comparison of *h*MDH1 and *h*MDH2: the insertion of two extra residues into the $\alpha7-\alpha8$ loop. This loop passes directly under the substrate binding pocket (D-malate in the *h*MDH2 ternary complex) and contributes the surface that underpins the bound substrate (Figure 4B). In addition to the insertion of two residues that results in a local shift in the registry, there are specific sequence differences ($^{hMDH1}Ile_{235}$ to Val; $^{hMDH1}Ser_{242}$ to Ala; $^{hMDH1}A_{243}$ to Thr) that alter the shape of the substrate binding pocket. There are also likely significant differences in the flexibility and dynamics of these two loop variants in response to ligand binding. While the malate binding pocket is small, these differences may afford an opportunity for selective small molecule inhibitor design.

3. CONCLUSIONS

The first overexpression, isolation, and purification of human MDH1 using a bacterial expression system have been described in detail. Further, the first *h*MDH1 crystal structure has been determined at a 1.65 Å resolution, with only a small molecule (malonate) bound in the active site. While the structure confirms that the enzyme is very similar to the previously reported porcine structure with which it shares a 95% sequence identity, this new structure without the bound NAD^+ cofactor provides some novel insights into the conformational flexibility of the enzyme. The $\beta4-\alpha4$ loop that cradles NAD^+/NADH in active enzymes adopts a conformation similar to that needed to bind NAD^+ in one crystallographic environment but is largely disordered in another. While crystallization can exaggerate the importance of conformations stabilized by crystal packing, it is possible that this range of motion is accessible to the protein in solution as well. A more open conformation suggestive of extensive protein flexibility has previously been observed in an *E. coli* MDH2 apo structure, (3HHP[8]), but not in any MDH1 structure. This flexibility may leave the enzyme susceptible to inhibition by small molecule dinucleotide mimetics that trap the enzyme in an inactive conformation.

The comparison of the *h*MDH1 structure to *h*MDH2 is also revealing. Distinct differences in these two enzymes in the vicinity of the substrate binding pocket might be exploited in the discovery of small molecules that inhibit human MDH1 with selectivity over the mitochondrial MDH2. This selectivity will almost certainly be a desirable attribute of any agent put forward for the clinical evaluation of the therapeutic potential of MDH1 inhibitors in the treatment of cancer. The

https://doi.org/10.1021/acsomega.1c04385
ACS Omega 2022, 7, 207−214

monoclinic *h*MDH1 crystal form reported here may be a particularly useful tool for use in future crystallographic fragment screening, specifically because of its extensively open and empty active site.

4. EXPERIMENTAL DETAILS

4.1. Reagents. Full-length *h*MDH1 was a gift of Dr. Ameeta Kelekar (University of Minnesota, Department of Immunology, Minneapolis, MN). A pGS-21a plasmid containing full-length *mdh*1 was purchased from GenScript. All enzymes used for DNA digestion were purchased from NEB (Ipswich, MA). All DNA purification kits were purchased from Qiagen (Venlo, Netherlands). Components necessary for protein production other than IPTG were ordered from VWR (Radnor, PA). HisTrap HP column for protein purification was purchased from formerly GE Life Sciences, now Cytiva (Marlborough, MA). All other materials necessary for protein purification and isolation, crystallization, and determination of enzymatic activity were purchased from Fischer Scientific (Waltham, MA).

4.2. Cloning, Expression, and Purification of Soluble His6-GST-*h*MDH1 Fusion Protein. The amino acid sequence corresponding to the full-length *h*MDH1$^{1-334}$ was codon-optimized and cloned into a pGS-21a plasmid with additional TEV protease cleavage sequence using *bgIII* and *XhoI* restriction sites. The purchased plasmid was transformed into competent Rosetta2-pLysS (BL21 DE3) cells and cultured on agar plates with Amp100 and Cm30. Colonies grew overnight, and a single colony was selected and shaken at 270 rpm overnight in LB media at 37 °C. One liter of LB media was inoculated with 3 mL of overnight colony and cultured until OD_{600} reached 0.5−0.7. The culture was cooled down for 1 h at 4 °C prior to being induced with 1 mM IPTG. Cultures were placed in a 20 °C incubator and allowed to shake for 16 h. Cells were harvested by centrifugation at 5000*g* for 15 min and stored at −20 °C overnight. The cell pellet was solubilized in buffer A (25 mM HEPES pH 7.2, 150 mM NaCl, 10 mM imidazole, and 5% glycerol). To this solution were added lysozyme (final concentration: 1 mg/mL) and 1.5 μL benzonase prior to sonication for 16 min (30 s on, 30 s off) at 30% attenuation. Lysed cells were distributed among 50 mL Beckman centrifuge tubes and centrifuged for 45 min at 45000*g*. The resulting supernatant was syringe-filtered (0.45 μm) and loaded onto a 5 mL HisTrap HP column. The fusion protein was eluted from the column using a linear gradient of buffer B (25 mM HEPES pH 7.2, 150 mM NaCl, 400 mM imidazole, and 5% glycerol). Like fractions were pooled together and TEV protease (8% w/w) was added before adding the protein solution to a dialysis cassette in TEV cleavage buffer (25 mM HEPES pH 7.2, 150 mM NaCl, 1 mM DTT, and 5% glycerol) at 4 °C overnight. Contents of dialysis tubing were syringe-filtered (0.45 μm) and loaded onto a HisTrap HP column to separate *h*MDH1 from the His-tagged fusion protein. Flow-through-containing *h*MDH1 was pooled together and concentrated to ≤5 mL prior to being syringe-filtered (0.22 μm) and loaded onto a Sephacryl S-100 column. Peaks from the size exclusion column were analyzed via SDS-PAGE, and the resulting *h*MDH1 was concentrated to 5 mg/mL in buffer supplemented with 10% glycerol. Aliquots were flash-frozen before being stored in a −80 °C freezer for future use. The resulting yield from the preparation was approximately 2.5 mg/L. The sequence was confirmed by crystallography and the function was confirmed via enzymatic activity assay.

4.3. Assessment of Enzyme Activity. Recombinant *h*MDH1 enzymatic activity was assessed by monitoring the time-dependent conversion of substrate oxaloacetate to malate. The parallel oxidation of NADH to NAD^+ was followed using an Agilent Technologies Cary Series ultraviolet−visible (UV−vis) spectrophotometer at 340 nm. NADH (100 μM) and oxaloacetic acid (240 μM) were added to cuvettes, mixed briefly, and the absorbance at 340 nm was measured at 10 s intervals over 10 min. The effect of enzyme on NADH conversion was determined by the addition of *h*MDH1 in a twofold dilution series (25−0.390625 nM) to prereferenced vials that were then monitored over the same time course. No change in absorbance was observed in a substrate-free control (25 nM NADH and *h*MDH1). Absorbance values were then converted to the concentration of NADH using Beer's law and the extinction coefficient for NADH (6.2 mM/cm). The initial linear portion of concentration versus time curves was entered in GraphPad Prism to determine the V_{max} and K_m values (Supporting Figure S2). Experiments were conducted in triplicate.

4.4. Crystallization. Protocols successfully used with *Sus scrofa* MDH1 served as a starting point for *h*MDH1 crystallization.[17] Microcrystals grew in 3−4 days by hanging drop vapor diffusion using a precipitant consisting of 25−30% PEG 4000, 100 mM citrate buffer pH 6.5, and protein-concentrated to 5 mg/mL in buffer containing 25 mM HEPES pH 7.4, 150 mM NaCl, and 10% glycerol. After several rounds of seeding and optimization, plate-like crystals (75 × 25 × 150 μm^3) reached full maturity within 48 h at 20 °C. Final conditions yielding monoclinic crystals were obtained by mixing equal amounts of protein with well solution containing 28% PEG 4000, 100 mM NaMalonate pH 7.2, and 0.15 mM ammonium acetate in 2 μL drops. Optimal cryo-conditions involved mother liquor plus 15% PEG 400.

4.5. X-ray Data Collection. Diffraction data was collected at IMCA-CAT beamline 17-ID at the Advanced Photon Source (APS), Argonne, Illinois. Data collection was completed at 100 K using a radiation of wavelength 1.00 Angstroms and a Dectris Eiger2 9M detector. Data was processed using *autoProc* and rescaled using *aP_scale* using R-factor (<0.4), completeness (>90%), and I/sigma (>2) as criteria, and a minimum of two of the three criteria were met in determining the proper resolution range.[21]

4.6. Structure Solution and Refinement. Due to the high sequence similarity between *Sus scrofa* MDH1 and *h*MDH1(95%), the *ss*MDH1 model, 5MDH (chain A) was used as the search model in molecular replacement with *Phaser*.[17,22] The monoclinic crystal was found to contain two protein chains in the asymmetric unit. Iterative rounds of refinement and model building were carried out using *Phenix*[23] and *Coot*.[24] Malonate was modeled into the corresponding electron density using standard geometry as in the *CCP*4 dictionary.[25] Refined structures were validated with *MolProbity*.[26] Supporting Table S1 summarizes statistics from the data collection and *Phenix* refinement for the assessment of the quality of the structures.[27] Molecular figures were made using the *PyMOL* Molecular Graphics System, Version 2.3 Schrödinger, LLC. Atomic coordinates and reflection data for *h*MDH1 with malonate bound in the substrate binding pocket have been deposited into the Protein Data Bank[28] (accession code: 7RM9).

https://doi.org/10.1021/acsomega.1c04385
ACS Omega 2022, 7, 207−214

■ ASSOCIATED CONTENT

Supporting Information

The Supporting Information is available free of charge at https://pubs.acs.org/doi/10.1021/acsomega.1c04385.

Crystallographic data and refinement statistics for *h*MDH1 (Table S1); omit map electron density surrounding the malonate molecule (Figure S1); B-value variability in the hMDH1 dimer (Figure S2) (PDF)

■ AUTHOR INFORMATION

Corresponding Author

Barry C. Finzel − *Department of Medicinal Chemistry, University of Minnesota, Minneapolis, Minnesota 55455, United States;* orcid.org/0000-0001-8761-3384; Email: finze007@umn.edu

Author

William M. McCue − *Department of Medicinal Chemistry, University of Minnesota, Minneapolis, Minnesota 55455, United States*

Complete contact information is available at: https://pubs.acs.org/10.1021/acsomega.1c04385

Notes

The authors declare no competing financial interest.

■ ACKNOWLEDGMENTS

W.M.M. was supported in this work by a Robert Vince Fellowship from the University of Minnesota Department of Medicinal Chemistry. This research used resources of the Advanced Photon Source, a U.S. Department of Energy (DOE) Office of Science User Facility operated for the DOE Office of Science by Argonne National Laboratory under Contract No. DE-AC02-06CH11357. Use of the IMCA-CAT beamline 17-ID (or 17-BM) at the Advanced Photon Source was supported by the companies of the Industrial Macromolecular Crystallography Association through a contract with the Hauptman-Woodward Medical Research Institute.

■ ABBREVIATIONS

GST, glutathione S-transferase; MDH, malate dehydrogenase; NAD, nicotinamide adenine dinucleotide; rmsd, root-mean-square deviation; TEV, tobacco etch virus

■ REFERENCES

(1) Sellés Vidal, L.; Kelly, C. L.; Mordaka, P. M.; Heap, J. T. Review of NAD(P)H-Dependent Oxidoreductases: Properties, Engineering and Application. *Biochim. Biophys. Acta, Proteins Proteomics* **2018**, *1866*, 327−347.

(2) Minárik, P.; Tomaásková, N.; Kollárová, M.; Antalík, M. Malate Dehydrogenases - Structure and Function. *Gen. Physiol. Biophys.* **2002**, *21*, 257−265.

(3) Wang, Y. P.; Zhou, W.; Wang, J.; Huang, X.; Zuo, Y.; Wang, T. S.; Gao, X.; Xu, Y. Y.; Zou, S. W.; Liu, Y.-B.; Cheng, J. K.; Lei, Q. Y. Arginine Methylation of MDH1 by CARM1 Inhibits Glutamine Metabolism and Suppresses Pancreatic Cancer. *Mol. Cell* **2016**, *64*, 673−687.

(4) Lunt, S. Y.; Vander Heiden, M. G. Aerobic Glycolysis: Meeting the Metabolic Requirements of Cell Proliferation. *Annu. Rev. Cell Dev. Biol.* **2011**, *27*, 441−464.

(5) Goldman, R. D.; Kaplan, N. O.; Hall, T. C. Lactic Dehydrogenase in Human Neoplastic Tissues. *Cancer Res.* **1964**, *24*, 389−399.

(6) Hanse, E. A.; Ruan, C.; Kachman, M.; Wang, D.; Lowman, X. H.; Kelekar, A. Cytosolic Malate Dehydrogenase Activity Helps Support Glycolysis in Actively Proliferating Cells and Cancer. *Oncogene* **2017**, *36*, 3915−3924.

(7) Beaupre, B. A.; Roman, J. V.; Hoag, M. R.; Meneely, K. M.; Silvaggi, N. R.; Lamb, A. L.; Moran, G. R. Ligand Binding Phenomena That Pertain to the Metabolic Function of Renalase. *Arch. Biochem. Biophys.* **2016**, *612*, 46−56.

(8) Zaitseva, J.; Meneely, K. M.; Lamb, A. L. Structure of Escherichia Coli Malate Dehydrogenase at 1.45 Å Resolution. *Acta Crystallogr., Sect. F: Struct. Biol. Cryst. Commun.* **2009**, *65*, 866−869.

(9) Hall, M. D.; Levitt, D. G.; Banaszak, L. J. Crystal Structure of Escherichia Coli Malate Dehydrogenase. A Complex of the Apoenzyme and Citrate at 1·87 Å Resolution. *J. Mol. Biol.* **1992**, *226*, 867−882.

(10) Cox, B.; Chit, M. M.; Weaver, T.; Gietl, C.; Bailey, J.; Bell, E.; Banaszak, L. Organelle and Translocatable Forms of Glyoxysomal Malate Dehydrogenase: The Effect of the N-Terminal Presequence. *FEBS J.* **2005**, *272*, 643−654.

(11) Gleason, W. B.; Fu, Z.; Birktoft, J.; Banaszak, L. Refined Crystal Structure of Mitochondrial Malate Dehydrogenase from Porcine Heart and the Consensus Structure for Dicarboxylic Acid Oxidoreductases. *Biochemistry* **1994**, *33*, 2078−2088.

(12) Kelly, C. A.; Nishiyama, M.; Ohnishi, Y.; Beppu, T.; Birktoft, J. J. Determinants of Protein Thermostability Observed in the 1.9-Å Crystal Structure of Malate Dehydrogenase from the Thermophilic Bacterium Thermus Flavus. *Biochemistry* **1993**, *32*, 3913−3922.

(13) Ferraris, D. M.; Spallek, R.; Oehlmann, W.; Singh, M.; Rizzi, M. Structures of Citrate Synthase and Malate Dehydrogenase of Mycobacterium Tuberculosis. *Proteins: Struct., Funct., Bioinf.* **2015**, *83*, 389−394.

(14) Huang, J.; Niazi, A. K.; Young, D.; Rosado, L. A.; Vertommen, D.; Bodra, N.; Abdelgawwad, M. R.; Vignols, F.; Wei, B.; Wahni, K.; Bashandy, T.; Bariat, L.; Van Breusegem, F.; Messens, J.; Reichheld, J. P. Self-Protection of Cytosolic Malate Dehydrogenase against Oxidative Stress in Arabidopsis. *J. Exp. Bot.* **2018**, *69*, 3491−3505.

(15) Rao, S. T.; Rossmann, M. G. Comparison of Super-Secondary Structures in Proteins. *J. Mol. Biol.* **1973**, *76*, 241−256.

(16) Birktoft, J. J.; Rhodes, G.; Banaszak, L. J. Refined Crystal Structure of Cytoplasmic Malate Dehydrogenase at 2.5-Å Resolution. *Biochemistry* **1989**, *28*, 6065−6081.

(17) Chapman, A. D. M.; Cortés, A.; Dafforn, T. R.; Clarke, A. R.; Brady, R. L. Structural Basis of Substrate Specificity in Malate Dehydrogenases: Crystal Structure of a Ternary Complex of Porcine Cytoplasmic Malate Dehydrogenase, α-Ketomalonate and TetrahydoNAD. *J. Mol. Biol.* **1999**, *285*, 703−712.

(18) Krissinel, E.; Henrick, K. Protein structure comparison service PDBeFold at European Bioinformatics Institute. http://www.ebi.ac.uk/msd-srv/ssm. Accessed Sept 3, 2021.

(19) Bergmeyer, H. U. *Methods of Enzymatic Analysis*; 2nd ed.; Elsevier, 1974.

(20) Dragovich, P. S.; Fauber, B. P.; Corson, L. B.; Ding, C. Z.; Eigenbrot, C.; Ge, H.; Giannetti, A. M.; Hunsaker, T.; Labadie, S.; Liu, Y.; Malek, S.; Pan, B.; Peterson, D.; Pitts, K.; Purkey, H. E.; Sideris, S.; Ultsch, M.; VanderPorten, E.; Wei, B.; Xu, Q.; Yen, I.; Yue, Q.; Zhang, H.; Zhang, X. Identification of Substituted 2-Thio-6-Oxo-1,6-Dihydropyrimidines as Inhibitors of Human Lactate Dehydrogenase. *Bioorg. Med. Chem. Lett.* **2013**, *23*, 3186−3194.

(21) Vonrhein, C.; Flensburg, C.; Keller, P.; Sharff, A.; Smart, O.; Paciorek, W.; Womack, T.; Bricogne, G. Data Processing and Analysis with the AutoPROC Toolbox. *Acta Crystallogr., Sect. D: Biol. Crystallogr.* **2011**, *67*, 293−302.

(22) McCoy, A. J.; Grosse-Kunstleve, R. W.; Adams, P. D.; Winn, M. D.; Storoni, L. C.; Read, R. J. Phaser Crystallographic Software. *J. Appl. Crystallogr.* **2007**, *40*, 658−674.

(23) Adams, P. D.; PV, A.; G, B.; VB, C.; IW, D.; N, E.; JJ, H.; LW, H.; GJ, K.; RW, G.-K.; AJ, M.; NW, M.; R, O.; RJ, R.; DC, R.; JS, R.; TC, T.; PH, Z. PHENIX: A Comprehensive Python-Based System for Macromolecular Structure Solution. *Acta Crystallogr., Sect. D: Biol. Crystallogr.* **2010**, *66*, 213−221.
(24) Emsley, P.; Lohkamp, B.; Scott, W. G.; Cowtan, K. Features and Development of Coot. *Acta Crystallogr., Sect. D: Biol. Crystallogr.* **2010**, *66*, 486−501.
(25) Winn, M. D.; Ballard, C. C.; Cowtan, K. D.; Dodson, E. J.; Emsley, P.; Evans, P. R.; Keegan, R. M.; Krissinel, E. B.; Leslie, A. G. W.; McCoy, A.; McNicholas, S. J.; Murshudov, G. N.; Pannu, N. S.; Potterton, E. A.; Powell, H. R.; Read, R. J.; Vagin, A.; Wilson, K. S. Overview of the CCP4 Suite and Current Developments. In *Acta Crystallographica Section D: Biological Crystallography*; International Union of Crystallography, April 18, 2011; Vol. *67*, pp 235−242.
(26) Chen, V. B.; Arendall, W. B.; Headd, J. J.; Keedy, D. A.; Immormino, R. M.; Kapral, G. J.; Murray, L. W.; Richardson, J. S.; Richardson, D. C. MolProbity: All-Atom Structure Validation for Macromolecular Crystallography. *Acta Crystallogr., Sect. D: Biol. Crystallogr.* **2010**, *66*, 12−21.
(27) Liebschner, D.; Afonine, P. V.; Baker, M. L.; Bunkoczi, G.; Chen, V. B.; Croll, T. I.; Hintze, B.; Hung, L. W.; Jain, S.; McCoy, A. J.; Moriarty, N. W.; Oeffner, R. D.; Poon, B. K.; Prisant, M. G.; Read, R. J.; Richardson, J. S.; Richardson, D. C.; Sammito, M. D.; Sobolev, O. V.; Stockwell, D. H.; Terwilliger, T. C.; Urzhumtsev, A. G.; Videau, L. L.; Williams, C. J.; Adams, P. D. Macromolecular Structure Determination Using X-Rays, Neutrons and Electrons: Recent Developments in Phenix. *Acta Crystallogr., Sect. D: Struct. Biol.* **2019**, *75*, 861−877.
(28) Berman, H. M.; Westbrook, J.; Feng, Z.; Gilliland, G.; Bhat, T. N.; Weissig, H.; Shindyalov, I. N.; Bourne, P. E. The Protein Data Bank. *Nucleic Acids Res.* **2000**, *28*, 235−242.
(29) Mueggler, P. A.; Wolfe, R. G. Malate dehydrogenase. Kinetic studies of substrate activation of supernatant enzyme by L-malate. *Biochemistry* **1978**, *17*, 4615−4620.

https://doi.org/10.1021/acsomega.1c04385
ACS Omega 2022, 7, 207−214